Long-term Effect of MPH on White Matter Tracts of Adults with ADHD

An Application of Consistent Model Selection followed by TBSS

Author:
Yulun Wu

Supervisor:
Dr. F.M. Vos
Daily Supervisor:
Ir. O.G. Filatova

Applied Physics
Faculty of Applied Sciences
Delft University of Technology

Long-term Effect of MPH on White Matter Tracts of Adults with ADHD

by

Yulun Wu

in partial fulfillment of the requirements for the degree of

Master of Science
in Applied Physics

at the Delft University of Technology,
to be defended publicly on Thursday June 21, 2018 at 9:00 AM.

Thesis committee:	Dr. F.M. Vos,	TU Delft & AMC, supervisor
	Ir. O.G. Filatova,	TU Delft, supervisor
	Prof. Dr. Bernd Rieger,	TU Delft
	Dr. Koen W.A. van Dongen,	TU Delft

Abstract

Attention-deficit/hyperactivity disorder (ADHD) is one common neuro-behavioral disorder, for which a commonly prescribed psychotropic drug is Methylphenidate (MPH). The effect of long-term medication use on white matter tracts is unclear. Diffusion tensor imaging (DTI) is an approach to research white matter properties by modelling the anisotropy of water diffusion. Tract-Based Spatial Statistics (TBSS) based on DTI is commonly used to perform a voxel-wise statistical analysis on a representation of white matter tracts. A framework based on a consistent model selection followed by modified TBSS shows an improvement of statistical power and a higher consistency of fiber property estimation in the crossing-fiber regions.

The aim of this thesis is to study the long-term effect of MPH on white matter tracts of ADHD patients with different medication duration. Two frameworks were applied to model the white matter based on DTI of the brains and for a voxel-wise statistical analysis. In the reference framework, we fitted the data to the single tensor model and modified the TBSS by using a high-dimensional registration. In the proposed framework, we fitted the ball-and-sticks model to the data and applied the consistent model selection (CMS) with the modified TBSS. A fiber orientation atlas constructed from our data improved the consistency of fiber orientation estimation by applying an orientation prior. Besides, we improved CMS by building the complexity atlas based on the improved fiber metrics, and by optimising the orientation prior to spatially localise the width of prior in each voxel. Intraclass correlation coefficient (ICC) calculated through separate fitting of four reproducibility datasets was used to evaluate the consistency of fitting with the optimised orientation prior.

In the voxel-wise statistical analysis of both frameworks, significant differences were not found among the white matter tracts of subjects under different duration of medication. Fitting with the optimised prior shows a higher ICC compared with the use of global fixed prior width during the fitting. In addition, applying CMS to another dataset appears an improved statistical power in fiber-crossings, which proves the generalizability of this pipeline.

In conclusion, no long-term effect of MPH was observed. We proposed the pipeline of CMS as a general pipeline to describe fiber-crossings in the white matter, with our improvements including the way calculating complexity atlas and the optimised orientation prior.

Acknowledgement

First of all, I would like to thank Lena Filatova and Frans Vos for their supervision and valuable scientific input to my master project, as well as for their affability to my everyday life. Next, I would like to thank Joor Arkesteijn for helping me with the model selection program. Furthermore, I would like to thank Tian, Ronald and Arno for their kindness to my questions related with the project. I would like to thank people from the master room for the interesting conversations during the breaks. Last but not the least, I would like to thank everyone in the Quantitative Imaging group for their friendliness.

Contents

Chapter 1

Introduction

Attention-deficit/hyperactivity disorder (ADHD) is one of the most common neurobehavioral disorders, characterized by inattention and/or impulsivity-hyperactivity [47]. Methylphenidate (MPH) is among the most commonly prescribed psychotropic drugs for treatment of ADHD [19]. Previous research shows that short-term MPH use leads to bigger changes in white matter characteristics in children compared with adults with ADHD [10]. The changes are related with white matter (WM) tract development. The influence of long-term treatment still needs to be investigated, based on a longer follow-up studies of ADHD patients with different medication duration.

To study WM structure, diffusion-weighted magnetic resonance imaging (DW-MRI) is commonly used, in which the anisotropy of water diffusion is measured to assess the local properties of local WM tracts [8]. Diffusion tensor imaging (DTI) is an approach to model DW-MRI, in which the anisotropy is modelled by the single tensor model (ST), which assumes a Gaussian diffusion profile [6]. Fractional anisotropy (FA) value is obtained from the diffusion tensor to describe the degree of directionality of WM structure.

To analyse and compare the FA images of different groups, Tract-based spatial statistics (TBSS) is a pipeline for multi-subject diffusion imaging analysis [38]. TBSS consists of a registration to establish spatial correspondence of all subjects in a common space, followed by a projection of FA values to a mean WM tract skeleton. However, [14] shows that optimised nonlinear image registration based on Elastix toolbox [23] without projection produces better alignment on the white matter skeleton than the registration-projection approach in TBSS.

It is well known that up to 90% of WM voxels contain more than one coherently orientated fiber population, which do not comply with the assumption of the single tensor model to represent the local diffusion behavior [2] [45]. In such voxels, it is not straightforward to evaluate the properties of WM based on FA. The reason is that spurious changes in the radial and axial diffusivity may be detected, which lack sensitivity of FA to detect changes in the white matter microstructure [46]. Metrics related with fiber population based on advanced models are needed for a meaningful analysis. To provide a more accurate description of diffusion in crossing-fiber regions, several models were proposed, e.g. the ball-and-sticks model [9], multi-tensor models [45] [12], or CHARMED [4]. These models describe the diffusion signal by modeling each fiber population separately, but require more extensive DW-MRI acquisition protocols. A model selection among the advanced models is needed to determine the number of fiber populations.

A framework was proposed to label the fiber populations based on their estimated orientations to analyze crossing-fiber regions of WM in TBSS [17]. However, it gives inconsistent labelling of fiber populations in every voxel, which leads to inconsistent modelled metrics of each fiber population across subjects. Recently, Dr. Joor Arkesteijn introduced a framework for consistent model selection (CMS) that enhances the consistency of diffusion model parameters and improves the statistical power in voxel-wise statistical analysis of crossing-fiber regions [3]. This is achieved by the introduction of an 'orientation prior' to promote inter-subject correspondence of estimated fiber orientations, and the application of a model complexity atlas to determine the number of fiber populations in a common space instead of in each subject. The construction of complexity atlas needs to be optimised, which does not take the advantage of the fiber properties estimated from CMS. Another limitation of CMS is the choice of the width of an Gaussian-shaped 'orientation prior'. In CMS, a fixed width of 'orientation prior' is used for all the voxels, which is too rigid for an adequate fitting. A voxel-wise width of 'orientation prior' needs to be defined.

In this thesis, we focus on the long-term effects of MPH on the human white matter tracts of adult patients with ADHD. The aim is to find out if there is a significant difference between groups including patients with different length of the medication use. We expect to see a bigger change of WM tracts of patients with long-term medication than others with shorter medication. We applied two frameworks. The reference framework (Section 3.2) consists of a modified TBSS based on single tensor fitting of DW-MRI data. The proposed framework (Section 3.3) includes the modified TBSS and the consistent model selection based on fitting the ball-and-sticks model to the data. We expect an enhanced model estimation and improved statistical power in fiber-crossings under the application of CMS.

Besides, we improved the CMS pipeline. First, we introduced an alternative way to build the complexity atlas based on the estimated fiber properties from the CMS (Section 3.3.6). We also optimised the orientation prior to spatially localise the width of orientation prior in each voxel, instead of a fixed width of the prior (Section 3.3.7). The improvement of fitting under the optimised orientation prior was evaluated by a reproducibility study. To prove the CMS pipeline is a general framework, we applied the CMS to another dataset to show the improved statistical power under application of CMS (Section 4.3). The result is valuable for an adequate clinical instruction.

Chapter 2

Theoretical Background

2.1 White matter in the brain

The central nervous system has two kinds of tissues: grey matter (GM) and white matter (WM). Grey matter, which has a pinkish-grey color in the living brain, contains the cell bodies, dendrites and axon terminals of neurons. On the other hand, white matter contains relatively few cell bodies and is composed mainly of long-range myelinated axon tracts. White matter forms the bulk of the deep parts of the brain and the superficial parts of the spinal cord. White matter is composed of bundles, which connect various grey matter areas of the brain to each other, and carry nerve impulses between neurons. Myelin (fatty white substance surrounding the nerve fibers) acts as an insulator, which ensures the quality of transmission of electrical signals. Myelin also increases the speed of transmission of all nerve signals by means of a conduction to allow electrical signals to jump, rather than course through the axon [7].

2.2 MRI basic theory

In magnetic resonance imaging (MRI), magnetic fields are used to manipulate and measure the magnetization of the nuclear spins in the body. Firstly, the nuclear spins are aligned in the direction of a strong static magnetic field (B_0 field, typically 1.5/3.0 Tesla). The nuclear spins (and therefore the magnetization) will start to precess around this B_0 field at a frequency known as the Larmor frequency, which is proportional to the field strength of B_0. Radio frequency (RF) fields are used to flip the magnetization into a plane that is transverse to the B_0 field. After the filpping induced by the RF field, the magnetization of each nucleus recovers from the excitation position to the original direction. This allows for measurement of the weak RF fields generated by the precessing spins using receive coils. Gradient coils are used to generate gradients along different directions in the static magnetic field and introduce a positional dependency of the precession frequencies:

$$\nu(\boldsymbol{r}) = \gamma(\boldsymbol{B}_0 + \boldsymbol{G} \cdot \boldsymbol{r}), \tag{1}$$

where ν is the precession frequency of nucleus with spatial position $\boldsymbol{r} = (x,y,z)$, γ is the gyromagnetic ratio scaled by $1/2\pi$, B_0 is the static magnetic field, $\boldsymbol{G} = (G_x, G_y, G_z)$. As a result, spatial positions are encoded by the gradients, which makes it possible to differentiate between signals coming from different positions in the body. Spatial localization of the measured MRI signal is enabled by means of slice-selection, frequency-encoding and phase-encoding. A pulse sequence consisting of a configuration of RF and gradient pulses is at the basis of different types of image contrast. For example, pulse sequences can be designed to generate contrast based on differences in the density of protons (PD), the decay rate of the transverse component of the magnetization (T2-relaxation), or the recovery rate of the parallel component of themagnetization (T1-relaxation). [33]

2.3 Diffusion weighted MRI

2.3.1 Diffusion in white matter

Particles are in constant motion in fluids at temperatures above absolute zero. This is also known as Brownian motion [11]. Due to collisions with other atoms and molecules, each atom or molecule makes random movements. In case of free diffusion, a Gaussian distribution describes the random displacements after a time t . The mean squared displacement is given by Einstein's equation:

$$\langle x^2 \rangle = 2nDt, \tag{2}$$

where n is the number of dimensions, D is the diffusion constant, and t is the diffusion time. Diffusion can be hindered due to presence of diffusion barriers, which results in shorter net displacements compared to free diffusion. For instance (Figure 1), in white matter the diffusion $(d_\perp)$ perpendicular to the axon orientation is hindered or restricted by the myelin sheaths around the axons, whereas diffusion$(d_{||})$ parallel to the axon orientation is relatively free. The degree of hindrance is orientationally dependent, which yields an anisotropic diffusion pattern. This anisotropic diffusion pattern is measured by applying a pulse sequence considering particle diffusion, which is explained below.

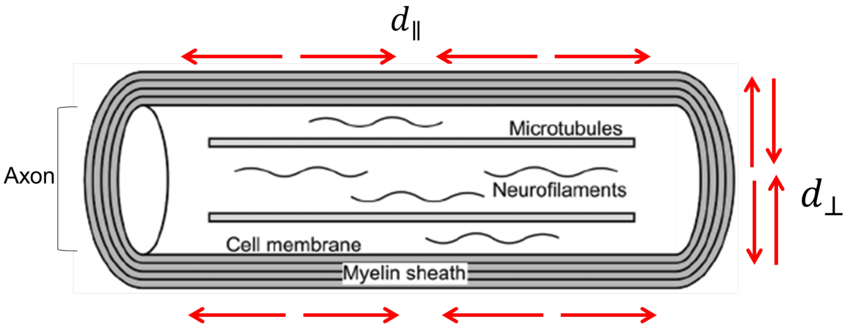

Figure 1: The diffusion in an axon (schematic drawing), adapted from [49]

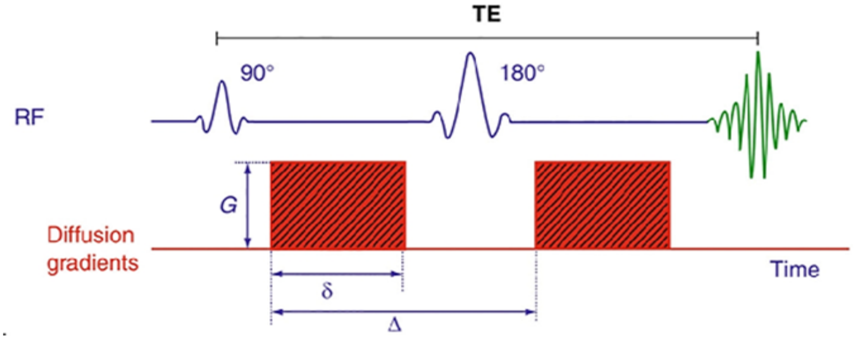

Figure 2: The PGSE pulse sequence from [40]

2.3.2 Pulsed gradient spin echo pulse sequence

The history of diffusion started from Hahn in 1950 [15] who observed the diffusion MRI signal. Torrey modelled the diffusion through a modification of the Bloch equations in 1956 [43]. Subsequently, Stejskal and Tanner introduced strong bipolar gradients in the pulse sequence to measure the diffusion in 1965 [39]. Their pulsed gradient spin echo (PGSE) pulse sequence is still widely applied nowadays as the bases for most diffusion-weighted MRI techniques.

The PGSE pulse sequence is shown in Figure 2. It contains a symmetric pair of diffusion-sensitizing gradients before and after the 180° RF pulse. This switching of gradients has no net effect in the case of a stationary spin, as the accumulated phase during the first gradient is compensated by the second gradient. However, for spins that diffuse along the gradient direction, a residual phase accumulates during the two gradient pulses. This difference in phase results in attenuation of the measured MR signal [27]. The larger the diffusion along the gradient orientation, the worse the rephasing and the more attenuation of the diffusion-weighted signal is observed.

2.3.3 Diffusion MRI signal

In case of Gaussian diffusion with apparent diffusion coefficient D, the diffusion-weighted signal S can be modelled as:

$$S = S_0 \exp(-bD), \tag{3}$$

where S_0 is the signal obtained without diffusion-sensitizing gradients, and b (also known as the b-value) is a parameter expressing the amount of diffusion weighting computed as:

$$b = \gamma^2 G^2 \delta^2 (\Delta - \frac{\delta}{3}), \tag{4}$$

where γ is the gyromagnetic ratio, G is the gradient strength, δ is the gradient duration of each diffusion-sensitizing gradient, and Δ is the time between the two diffusion-sensitizing gradients. In the brain regions of the CSF and the grey matter, the diffusion-weighted MRI signal is relatively independent of the orientation while in the white matter, the diffusion-weighted MRI signal depends strongly on the gradient orientation due to the anisotropic diffusion. Higher b-value results in higher diffusion contrast while decreasing the SNR of the image.

2.4 Diffusion tensor imaging

The diffusion MRI signal modelled as an exponential with a single scalar ADC is only true in tissue with isotropic diffusion. If we want to describe anisotropic diffusion, such as in white matter bundles, the 3D diffusion profile needs to be taken into account [5]. The diffusion tensor (DT) models the diffusion profile as an ellipsoid by assuming a single Gaussian diffusion process in a voxel. The DT is described by a 3 x 3 matrix [6]:

$$D = \begin{pmatrix} D_{xx} & D_{xy} & D_{xz} \\ D_{yx} & D_{yy} & D_{yz} \\ D_{zx} & D_{zy} & D_{zz} \end{pmatrix} \tag{5}$$

with the diagonal elements representing the ADC in three orthogonal directions and the off-diagonal elements representing the correlations between the diffusion of corresponding directions. In general, the orthogonal directions (*x,y,z*) are aligned with the magnetic field gradients of the MR-system [26]. The matrix is symmetric so that only six elements are independent. Thus the DT can be estimated by solving a linear system of seven acquisitions which consist of 6 acquisitions with non-colinear gradient directions and a b_0 acquisition to estimate the non-diffusion weighted signal. The eigenvectors and eigenvalues of the DT are used to describe the microstructure of a tissue in a voxel. Particularly, the first eigenvector defines the orientation of the fiber axons while the eigenvalues are used to calculate rotationally invariant measures such as the degree of anisotropy (fractional anisotropy or FA) and mean diffusivity (MD) [31]. The FA and MD are defined as:

$$FA = \frac{\sqrt{3\sum_{i=1}^{3}(\lambda_i - \overline{\lambda})^2}}{\sqrt{2\sum_{i=1}^{3}\lambda_i^2}} \tag{6}$$

$$MD = \frac{\lambda_1 + \lambda_2 + \lambda_3}{3} \tag{7}$$

where λ_i denotes the i-th eigenvalue of the DT and FA $\in [0, 1]$.

DTI is widely used in the field of neuroscience, especially for reconstructing WM pathways from estimated fiber orientations using fiber tractography. Furthermore, the scalar measures can be used to investigate the progress of diseases such as multiple sclerosis, Parkinson's disease, Alzheimer's disease and autism, and the effects of education and aging on the brain [21].

2.5 Diffusion models

2.5.1 The Single Tensor model and limitations

In the DTI, the diffusion tensor (DT) models the diffusion profile as an ellipsoid, which is also known as the single tensor model (ST). The single tensor model has the assumption of a single Gaussian diffusion process in a voxel. Thus, the single tensor model has several limitations. It does not hold in voxels with multiple fiber populations where non-Gaussian diffusion is observed [45]. The prevalence of multi-fiber voxels has been estimated to range from 33% up to 90% of the WM voxels [9] [20]. Consequently, DTI-based tractography leads to erroneously reconstructed WM pathways. Moreover, scalar variables are estimated ambiguously. For example, in a voxel with two crossing fibers, the FA measured using DTI will be unexpectedly decreased if there is an increase in the FA of one fiber population [13].

2.5.2 Advanced diffusion models

Methods to address the issue of multiple fiber populations in a voxel are used, for example, modelling the signal coming from different fiber compartments [9] [45] [51] [4] [25]. To apply these methods, a more complicated data acquisition has to be used. For example, a larger number of gradients for a single b-value (High angular resolution diffusion imaging or HARDI) [45] or sampling the space of diffusion weightings b (q-space) in some other fashion [44] can be implemented.

For modeling the signal from multiple fiber populations, a general signal model can be defined as a combination of signals from different fiber bundles and extra-axonal compartments:

$$S = (1 - f) \sum_i v_i S_{fiber,i} + f S_{extra-axonal}, f \in (0, 1) \tag{8}$$

where S_{fiber} and $S_{extra-axonal}$ denote the signal arising from the fiber and extra-axonal compartments, f stands for the volume fraction of the extra-axonal compartment and v_i represents the volume fraction of each fiber compartment.

2.6 Image registration

Image registration is an important tool in the field of medical imaging. In many clinical situations, several images of a patient are made in order to analyse the patient's situation. These images are acquired with multi-modalities (X-ray scanners, Magnetic Resonance Imaging (MRI) scanners, Computed Tomography (CT), etc), with a single modality but different scanners, at different moments of time or in different patient's conditions. Combination of these images for a patient often yields additional clinical information not apparent in a separate image. For this purpose, the spatial relation between the images has to be found.

Two images with the same dimension are involved in the registration process: the moving image $I_M(x)$ is aligned to fit the fixed image $I_F(x)$. The problem of registration is finding a transformation $\boldsymbol{T}(x) = x + u(x)$ which allows to achieve the alignment (equation 9).

$$I_M(\boldsymbol{T}(x)) = I_F(x), \boldsymbol{T} : \Omega_F \in \mathbb{R}^d \to \Omega_M \in \mathbb{R}^d \tag{9}$$

The quality of the alignment is defined by a distance or similarity measure S,

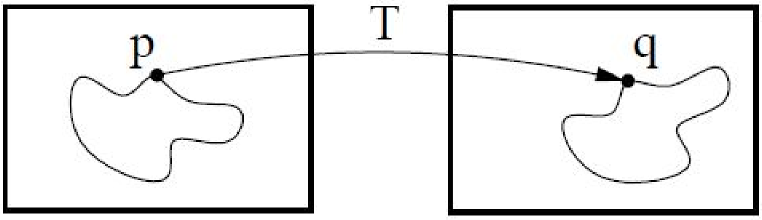

Figure 3: The task of image registration is finding a spatial transformation mapping from one image to another. Left is the fixed image and right the moving image, adapted from [22]

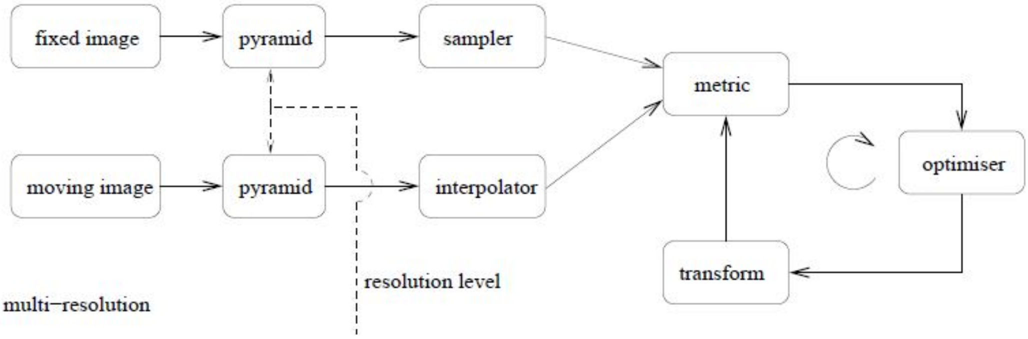

Figure 4: The main components of a registration algorithm in a block scheme from [23]

for instance, the sum of squared differences (SSD). Because this problem is ill-posed for nonrigid transformations $\boldsymbol{T}$, a regularisation or penalty term $\mathcal{P}$ is often introduced to constrain $\boldsymbol{T}$. Generally, the registration problem is formulated as an optimisation problem in which the cost function $\mathcal{C}$ is minimised:

$$\hat{\boldsymbol{T}} = \arg\min_{\boldsymbol{T}} \mathcal{C}(\boldsymbol{T}; I_F, I_M) \tag{10}$$

$$\mathcal{C}(\boldsymbol{T}; I_F, I_M) = -\mathcal{S}(\boldsymbol{T}; I_F, I_M) + \gamma\mathcal{P}(\boldsymbol{T}) \tag{11}$$

where γ weighs similarity against the penalty term.

2.6.1 Components of registration

Figure 4 shows the general components of a registration algorithm in a block scheme [16]. At the beginning of the scheme, the images are smoothed or down-sampled with multi-resolution strategies to speed-up registration and make the registration robust. At each resolution level for the fixed image, a subset of all the voxels is selected with a certain sampler [24] for the calculation of cost function. At each iteration the value of the cost function (metric) is calculated. If the metric is not minimized, an optimiser is used to update the parameters in the transformation. Iterations are needed until the solution of Equation (10) is found. For the moving image, the value of $I_M(\boldsymbol{T}(x))$ is evaluated at non-voxel positions during the updating step of the optimisation, for which intensity interpolation is needed. The details about the main components of registration is below:

1. Cost function

   The mean squared difference (MSD), normalized correlation (NC), mutual information (MI) are common choice of cost functions. MSD is only suited for images from the same modality while NC assumes less strict affine relation between the intensities of the images. MI is a recommended cost function [22], because it only assumes a statistical relation between the intensities of the images which can apply for images from single or multiple modalities.

2. Transformation

   For a linear transformation, it warps the moving image and make the alignment (Equation (12)). For example the affine transformation with 12 degrees of freedom allows for rotation, shear, scaling and skew of images. Here A is a matrix and t represents a translation vector.

   $$T_\mu(x) = Ax + t \tag{12}$$

   A linear transformation is needed only for a coarse registration. Sometimes the differences between subjects are such that the linear transform is not sufficient to achieve good registration. A non-linear transformation initialized with a linear transformation is used for to permit the local deformations from the moving image to the template. Using a nonlinear transformation directly might result in finding the local minimum solution instead of the global minimum, thus the moving image is over warped to fit the fixed image. A commonly used non-linear transformation is B-spline transformation. The B-spline transformation is modelled as a weighted sum of the cubic multidimensional B-spline polynomial [34]. The amount of spacing between the control points defines the complexity of the transformation.

3. Optimisation

   In Figure 4, we have mentioned an iterative optimisation procedure to solve

Equation (10). The commonly used optimisation is the gradient descent method (Euqation (13)). The subscript k mean in a certain iteration k. The parameters of transformation in iteration k is μ_k, which are updated by taking a step in the search direction d_k with a step size a_k.

$$\mu_{k+1} = \mu_k + a_k d_k \tag{13}$$

Usually the search direction is the derivative of the cost function $\frac{\partial C}{\partial \mu}$ evaluated at the current position μ_k. Different definitions of a_k and d_k yield different types of optimisation methods.

4. Sampler

   To compute the cost function, a set of voxels needs to be selected. The sampler component in Figure 4 is responsible for this. The most straightforward strategy is to use all voxels from the fixed image which will be very time-consuming for large images. Using only a small random subset (≈ 2000 voxels) from the fixed image accelerates registration significantly, without compromising registration accuracy [24]. And random sampling off the voxel grid has been shown to improve the smoothness of the cost function [30] [41].

5. Interpolator

   An intensity interpolation is needed for computation of the cost function since the value of transformed moving image is evaluated at nonvoxel positions. An additional interpolator is needed to accommodate the off-voxel random coordinate sampler. Several methods of interpolation exist, varying in quality and speed, including nearest neighbor, linear and n-th order B-spline interpolation [41] [42].

6. Hierarchical strategies

   A hierarchical (multi-resolution) strategy starts the registration process using images with lower complexity of resolution. A certain multi-resolution image pyramid is applied for smoothing and down-sampling and a series of images with increasing amount of smoothing are produced for registration with different image resolution. This increases the chance of successful registration [29] and reduces the computation time.

2.7 Tract based spatial statistics

As we mention in Section 2.4, fractional anisotropy (FA) is one of the measures commonly derived from diffusion MRI data, which quantifies how strongly directional the local white matter structure is. TBSS is a pipeline to provide a solution to the alignment of FA images from multiple subjects, which allows valid voxelwise analysis. It uses an adjusted non-linear registration followed by projection onto an registration-independent tract representation of white matter. The default TBSS pipeline consists of four steps as implemented in FSL [18], which will be implemented as follows.

The first step is a carefully tuned non-linear registration. The cost function consists of a similarity measure with a 'sum-of-squared difference' and a regularization term on the transformation field. The transformation is B-Splines transformation optimised by moving the control point locations until the regularization term (in cost function) is minimized. The control point spacing is set to 20 mm for achieving an appropriate degree of warp complexity, i.e., capability of high-dimensional warping also preserving structure topology of the original images. The nonlinear registration is preceded by affine registration, to achieve initial alignment. At the end of this step, all the images are warped into a common space defined by the chosen template.

Subsequently, the mean of all aligned FA images is created. The mean FA image is skeletonised to represent the center of all tracts which are common to all subjects. To make the FA skeleton, the local tract perpendicular directions are estimated at all voxels in the image. A search is made along all voxels in the local tract perpendicular direction, and the voxel with the highest FA is identified as the centre of the tract [38]. Usually the skeleton should be thresholded to excludes voxels which are primarily grey matter or CSF.

In the projection step, for each subject, we search in the perpendicular tract direction (computed in last step) of the mean skeleton to find the maximum FA value. This value is used to assign the skeleton voxel so that each subject's FA image is skeletonised. The aim of the projection step is to eliminate the residual misalignments between subjects after the non-linear registration. The skeletonised FA images are used in the following voxel-wise statistics.

2.8 Permutation testing based on the general linear model

To determine whether there are significant differences between the groups receiving different treatment, permutation testing is applied to the data modelled by the general linear model (GLM). A general linear model [36] at each spatial point of an image representation can be formulated and expressed as a weighted linear sum of experimental regressors. These modelled regressors are included in a design matrix. The GLM fitting is used to estimate to what extent of relationship between the modelled responses and the actual responses in each voxel.

After applying the GLM, a permutation testing follows. In each voxel, a certain test statistic T (t-test, F-test, etc) is calculated. A particular observed value T_0 of this statistic after the experiment has been conducted. After that the labels from the original data are shuffled and the statistic is calculated again. A number of permutations of the dataset result in a distribution of the statistic. We define the p-value as the probability of observing, by chance, a test statistic equal or larger than the one computed with the observed value, i.e. $P(T \geq T_0)$. Under the null hypothesis, there is no significant difference between the datasets. Given a significance level α, we reject the null hypothesis if p-value is less than α and conclude that there is significant evidence against the null hypothesis at level α. The permutation test is performed under the assumption that certain groups of labels must be exchangeable without consequences under the null-hypothesis.

Chapter 3

Methods

3.1 Data

3.1.1 Study population

In this study, adult subjects suffering from ADHD were included based on the length of period they were treated with MPH. The demographic details of three groups are shown in Table 1. In total, 84 subjects were included, uniformly distributed in three groups approximately (29 subjects in Group1, 26 subjects in Group2, 29 subjects in Group3). The patients in Group1 did not receive medication. The patients in Group2 received medication, with longer duration (over ten years) and earlier starting age compared to the patients in Group3. We refer to these as long-term medication users. Subjects in Group3 were exposed to medication for under one year. We refer to these as short-term medication.

	Age	Start age	End age
Group1	28.6±4.6		
Group2	25.9±2.8	9.1±2.8	19.8±2.9
Group3	28.6±4.8	27.9±4.5	28.6±4.8

Table 1: Information of patients in three groups in the dataset. All values are mean ± SD. Start/End age means the age when a patient started/finished using the medication.

3.1.2 Data Acquisition

All MR images were acquired with a 3.0 T Philips MR scanner equipped with a SENSE 8-channel head coil and body coil transmission (Philips Medical Systems, Best, The Netherlands). DWIs were acquired with a single shot, diffusion-weighted spin echo echo planar imaging sequence using a repetition time TR = 8135 ms and TE = 94 ms. The slice thickness is 2mm, thus a native voxel size is 2 mm x 2 mm x 2 mm. DWIs were acquired in 32 non-collinear directions with a b-value of 1000 s/mm^2. One volume was acquired without diffusion weighting (the b0-volumes). The field of view is 224 mm x 224 mm.

3.1.3 Preprocessing of diffusion weighted data

The acquired DWIs were corrected for motion and eddy current distortions by affine registration of DWIs to the acquired b_0 image with FLIRT in FSL [18]. The b_0 image is the image without diffusion sensitizing magnetic gradient (b-value equals to 0). After registration to the b_0 image, the gradient directions were reoriented according to the rotation component of the transformation matrix of the affine registration (12 degree of freedom) [28]. We apply BET [37] brain extraction to the non-diffusion-weighted image to exclude non-brain voxels from further consideration. This brain mask was applied to diffusion-weighted images.

3.2 Reference frameworks

3.2.1 The modified TBSS analysis

The reference framework (Figure 5) essentially performed a TBSS pipeline with modified registration procedure based on the single tensor model. The aim was to evaluate the difference between the voxel-wise FA value of subjects in different groups. In modified TBSS, we use a high-dimensional registration, instead of coarse registration combined with a projection step in default TBSS. After the preprocessing of the data, the single tensor model was fitted to the DWIs at each voxel using fit_MRI [32]. Based on this model, voxel-wise maps of FA values were calculated. A spatial normalization was achieved by applying registration from the FA images to a common space. We used Elastix [23] as the tool to realise a high-dimensional registration. Next, the aligned FA images were ‘skeletonised’ by the TBSS created white matter skeleton. A voxel-wise statistical analysis was performed to evaluate the group differences, shown in Section 3.3.9. The details of the Elastix settings are describe in the next section.

3.2.2 Registration by Elastix

Elastix was selected to align the FA images to the atlas space (dimension is $1 \times 1 \times 1$ mm^3). The template we use was FMRIB58_FA in FSL [18]. Under the multi-resolution strategy, the FA images with a certain resolution were used as an input to the sampler and the corresponding value of cost function was evaluated. Next the procedure of optimisation and transformation followed by evaluation with metrics were iterated, as a common registration scheme does.

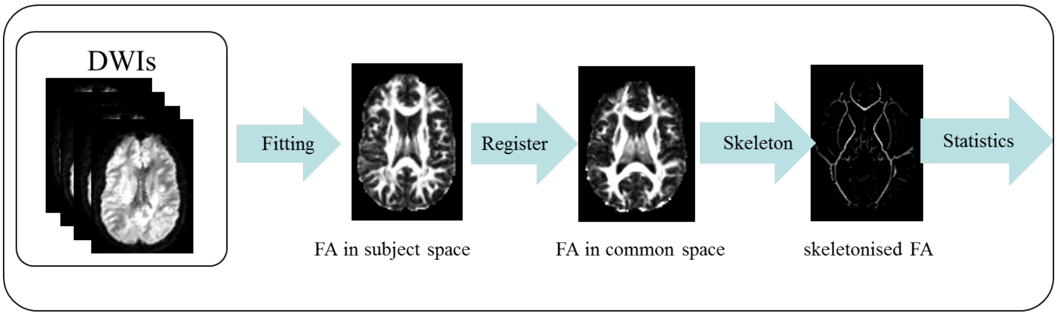

Figure 5: The reference framework performs a modified TBSS analysis in each subject. After fitting the single tensor model to the DWIs and compute the FA in each voxel, the FA image was aligned to a common space defined by a template. Subsequently, aligned FA image was skeletonised for a voxel-wise statistical analysis.

Our choice of configurable settings for the registration is described below. We chose MI/NCC as the cost function and for each choice of cost function we selected different number of voxels (2000-4000) in the random coordinate sampler. For each subject, we used Affine transformation for initialization followed by a B-spline transformation. The four resolutions of the B-spline grid are set to [64 32 16 8] mm. For the multi-resolution strategy, a Gaussian image pyramid [29] was applied for both the fixed and the moving image, which applied smoothing without down-sampling. Four resolutions were used, as this seemed to be a good trade-off between speed and accuracy [23].

3.3 Proposed framework

The proposed framework demonstrated a pipeline of consistent model selection (CMS). An overview of the proposed framework is shown in Figure 6, as adapted from [3]. A fiber orientation atlas was constructed based on the model parameters from automatic relevance determination (ARD) in FSL [18] to estimate mean fiber orientations across all the subjects. We also computed a model complexity atlas to determine the number of fiber populations in each voxel not depending on one subject, but on all the study populations. The ball-and-sticks models (Section 3.3.1) with one or two stick compartments were fitted to the diffusion-weighted images (DWIs). The orientation atlas was used as prior during the fitting of ball-and-2sticks model. Next, the ball-and-sticks model parameters were warped into a common space (defined by atlas from the IXI dataset [50]). An adjusted TBSS pipeline was used to skeletonise the estimated partial volume fractions (PVFs) of fibers in each voxel. The different skeletonized datasets were merged according to the complexity atlas: in single fiber voxels the first PVF was taken from the ball-and-one stick model fitting and the sec-

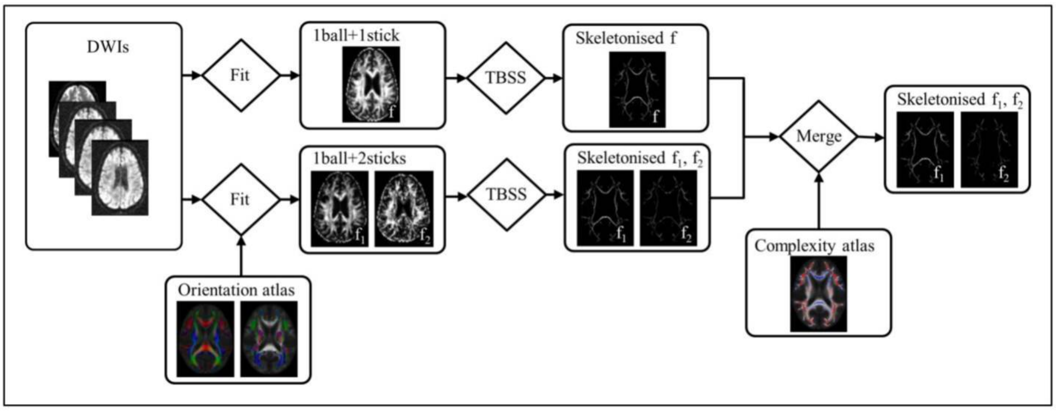

Figure 6: The proposed framework, adapted from [3]. The ball-and-sticks models were fitted to diffusion-weighted images (DWIs) per subject. An orientation prior was used to initialize the fitting and acted as an orientation prior to regularise the fitting. The PVFs (f1 for the PVFs of primary fiber populations, f2 for the PVFs of secondary fiber populations) were warped and skeletonised using a modified TBSS. In the common space, the different skeletonised datasets were merged according to a complexity atlas, such that two skeletonised datasets remained. In single-fiber and crossing-fiber voxels (according to the model complexity atlas) the two skeletonised datasets contained PVFs from the ball-and-one-stick and the ball-and-two-sticks model respectively.

ond PVF was set to zero; in two-fiber skeleton voxels the PVFs originated from the ball-and-two-sticks model. As a consequence, consistent model selection was enforced across the subjects of the study population, followed by statistical analysis.

3.3.1 The ball-and-sticks model

The diffusion-weighted signal S_θ was modelled according to the ball-and-sticks model [18]:

$$S_{\theta,i} = S_0 \left((1 - \sum_{j=1}^{N} f_j) \exp(-b_i d) + \sum_{j=1}^{N} f_j \exp(-b_i d (\boldsymbol{V}_j \cdot \boldsymbol{g}_i)^2) \right) \tag{14}$$

where $S_{\theta,i}$ is the i-th diffusion-weighted signal under b_i, b_i is the diffusion-weighting parameter, $\boldsymbol{g}_i$ is a unit vector that specifies the direction of the diffusion-encoding gradient pulses, S_0 is the non diffusion-weighted signal, N is the number of stick compartments (0, 1 or 2 in this research), d is a diffusivity parameter, f_j is the partial volume fraction (PVF) and $\boldsymbol{V}_j$ the principal eigenvector of the j-th stick compartment. The eigenvectors $\boldsymbol{V}_j$ are parameterized using spherical coordinates ψ_j and ϕ_j.

3.3.2 Automatic relevance determination

The computation of fiber orientation atlas and model complexity atlas was based on the automatic relevance determination (ARD). The ARD framework [18] was used to estimate the model parameters as well as to achieve an automatic model selection from the ball-and-sticks models. After fitting ball-and-2sticks model based on a Bayesian approach, two partial volume fractions (PVFs) and fiber orientations were obtained. A shrinkage prior was used to automatically reduce the volume fraction of the secondary fiber population to zero when it is not supported by the data, by which it achieves an automatic model selection from the ball-and-sticks model with one or two stick compartments. The ARD is available through the function bedpostx in FSL [18].

3.3.3 Construction of the fiber orientation atlas

To construct the orientation atlas, firstly, the single diffusion tensor model was fitted to all 84 subjects of the dataset available through the fit_MRI toolbox. A maximum likelihood estimation [32] was used for the fitting process. DTI-TK was used to register the diffusion tensor images from all subjects to a population-specific template using the full diffusion tensor information [52]. A transformation was computed from subject space to the common space. Subsequently, the PVFs and the corresponding stick orientations computed from ARD were warped to the common space by ‘deformationScalar3DVolume’ and ‘deformationSymTensor3DVolume’ functions in DTI-TK. The PVFs of fiber populations smaller than 0.05 were discarded [18]. Each voxel could contain 0, 1 or 2 fiber populations.

For the computation of the fiber orientation atlas, a clustering routine was used to compute the mean fiber orientation in the study population for both primary and secondary fiber polulation in each voxel. The mean fiber orientation of every cluster was computed by an adapted K-means clustering routine (K=2), which minimized the sum of squared angular differences under the assumption of 180° symmetry:

$$J = \sum_{k=1}^{2} \sum_{i \in C_k} \arccos(|\boldsymbol{V}_i \cdot \boldsymbol{V}_{k,mean}|)^2, \tag{15}$$

where C_k is the k-th cluster, V_i the i-th fiber orientation in C_k, and $V_{k,mean}$ the average fiber orientation of all fiber orientations in C_k. In the initialization step, the primary and secondary fiber orientations in each voxel for all the subjects were clustered into two groups from which the average fiber orientations were computed. The clustering routine was initialized by assigning all larger stick compartments to the first cluster and all smaller stick compartments to the second cluster. In the update step, the mean orientation of each cluster was obtained by first computing the scatter matrices S_k [35]:

$$S_k = \sum_{i \in C_k} \boldsymbol{V}_i \cdot \boldsymbol{V}_i^T, \tag{16}$$

The scatter matrix is the sum of dyadic products of the fiber orientations in C_k. The average fiber orientation $V_{k,mean}$ was updated as the eigenvector corresponding to the largest eigenvalue of the matrix S_k. In the assignment step, each fiber orientation was assigned to the mean orientation with which this fiber had the smallest angle (assuming under 180° symmetry). The clusters of the primary and secondary fiber orientation were updated. The update and assignment step were iterated until no fibers changed clusters.

3.3.4 Computation of the complexity atlas

The model complexity atlas was defined as the average number of fiber populations in each voxel. Based on the ARD, the PVFs in each voxel were calculated. For both primary and secondary fiber populations, we recognized PFV above 0.05 as a fiber population. We binarised the PVF image based on this threshold to transfer the volume fraction into number of fiber populations. After that, we did a majority voting of the number of fiber populations in each voxel based on all the subjects in our study. To obtain a discrete model complexity atlas, the average number of fiber populations was thresholded at 1.5 (we consider the area with a value above 1.5 as the crossing-fiber region). As a result, the model complexity atlas was used to achieve the model selection.

3.3.5 Model estimation with prior

The ball-and-one-stick model was fitted without using any prior information on the stick's orientation. The ball-and-two-sticks model was fitted using the fiber orientation atlas as a prior. It can enhance the fitting in two ways: (1) the atlas orientation was used to initialize the non-linear fit, and (2) a Gaussian-shaped prior $p(\theta)$ was applied to regularize the fitting of the model:

$$p(\theta) \propto \exp\left(-\frac{\epsilon_1^2}{2\sigma_\theta^2}\right) \exp\left(-\frac{\epsilon_2^2}{2\sigma_\theta^2}\right) \tag{17}$$

with

$$\epsilon_i = \arccos(|\boldsymbol{V}_i \cdot \boldsymbol{V}_{i,mean}|), \tag{18}$$

where $\epsilon 1$ and $\epsilon 2$ represent the angles between the principal eigenvector of both sticks and their corresponding atlas orientations, and σ_θ denotes the width of the Gaussian-shaped orientation prior. The estimated model parameter θ is given by:

$$\hat{\boldsymbol{\theta}} = \arg\max_{\theta} \log p(S|\boldsymbol{\theta})p(\boldsymbol{\theta}), \tag{19}$$

which was implemented using the fit_MRI toolbox. In each voxel, we considered the angle between the primary or secondary fiber sticks and the mean fiber orientation following a Gaussian distribution. And the width of the Gaussian-shaped orientation prior was set to 20° as a default value in fit_MRI toolbox. Another function of using the orientation atlas as a prior was to reassign the first and second fiber population. The PVFs in the ball-and-two-sticks model were implicitly sorted in subject space by means of the orientation prior.

3.3.6 An alternative way to build the complexity atlas

Previously, we build the complexity atlas based on PVFs from automatic relevance determination, not from CMS. We proposed building the complexity atlas in a different way. Since after fitting with an orientation prior in the pipeline of CMS, the diffusion model parameters including the PVFs were enhanced. Also under the application of orientation atlas, the labeling of the primary and secondary fiber populations became more consistent, which correspondingly enhanced the labeling of the PVFs for each fiber population. Thus, we built the model complexity atlas based on the PVFs from the pipeline of CMS. We expected this rebuilt complexity atlas different from the one we built previously to decide the number of fiber populations in each voxel.

3.3.7 Optimising the orientation prior

We optimised the orientation prior by localising the width of prior (σ_θ) in each voxel. During the construction of the orientation atlas, we obtained the distribution of the included angles between fiber orientation from each subject and mean fiber orientation in each voxel. We calculated a standard deviation map for the whole brain as a localised σ_θ based on this distribution. We expected a more consistent fitting with this optimised orientation prior.

To evaluate the fitting based on a different fixed values of σ_θ and the localised σ_θ, we produced four reproducibility datasets. The evaluation framework is shown in Figure 7. In each subject, the data was bootstrapped by keeping the b_0 image and randomly choosing 75% of DWIs. This was repeated for four times. The same bootstrapped pipeline was also applied for all the subjects, to obtain four reproducibility dataset. Next, each subject in four datasets were fitted with an orientation prior a fixed width of σ_θ (from 10° to 60°) as well as a σ_θ with localised width in each voxel. To evaluate the consistency of modelling primary/secondary fiber volume fraction, intraclass correlation coefficient (ICC) was calculated as a function of σ_θ in each voxel. The calculation of ICC considered 'between row variance' (indicating the variance for testing reliability of different subjects) and 'within row variance' (indicating mean level of testing reliability across all subjects).

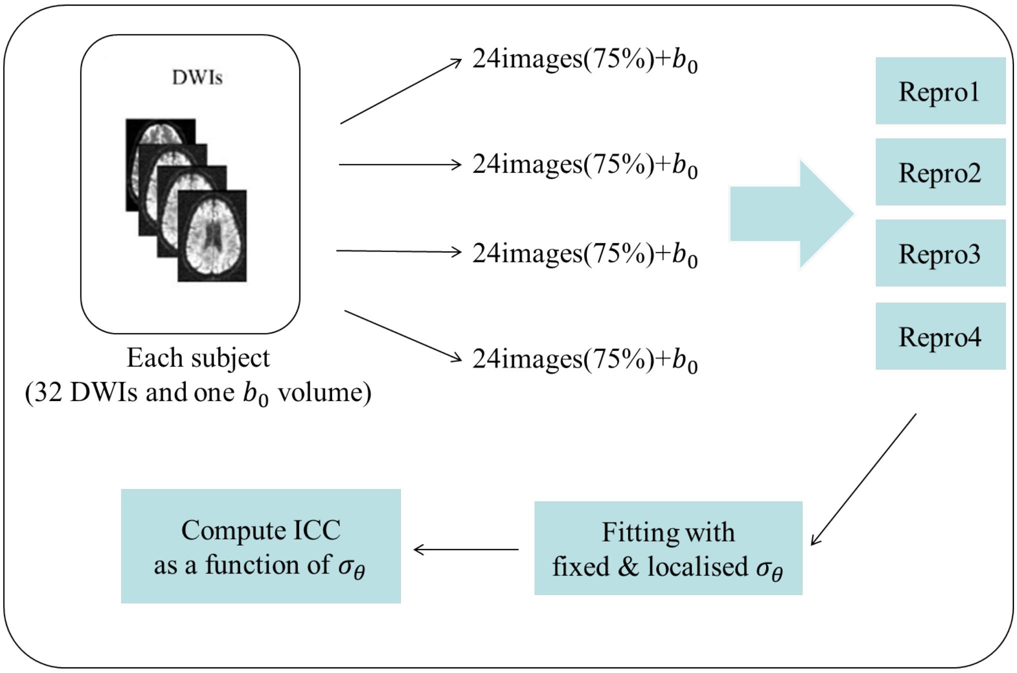

Figure 7: The framework to evaluate the choice of σ_θ. 'Repro' mean a reproducibility dataset. For each subject, 75% of the DWIs were randomly selected for four times, which were defined as reproducibility datasets. During the fitting of each dataset, a fixed prior width (10°,15°,20°,25°,30°,35°,40°,50°,60°, respectively) and a localised prior width were applied. ICC was computed across four datasets for each application of a prior width.

3.3.8 The modified TBSS analysis

The PVFs of the primary and secondary fiber populations after fitting the ball-and-sticks models were warped into the atlas space. According to the TBSS pipeline, the FA images created from the reference framework were averaged after which a skeleton was generated with the function tbss_skeleton (in FSL). The mean FA skeleton was thresholded at 0.2 merely to exclude voxels with large intersubject variability and/or partial volume effects with grey matter or cerebrospinal fluid. This skeleton was binarised to mask the FA images and the PVFs for obtaining skeletonised data. Since DTI-TK performed a high dimensional registration, we ignored the 'maximum skeleton projection' step of a standard TBSS analysis [38]. Finally, the skeletonised datasets from the two models were merged according to the model complexity atlas: in the single fiber voxels, the primary PVF from the ball-and-one-stick model was obtained and the secondary PVF was set to zero; in the two-fiber voxels, the PVFs were received from the fitting of the ball-and-two-stick diffusion model.

3.3.9 Statistical analysis on white matter tracts

Up to this step, we already had skeletonised data of FA and PVFs. The FA data was under the modified TBSS with different registration components. The PVFs data was from normal consistent model selection (CMS), from CMS with the complexity atlas calculated as we proposed and from CMS with an optimised orientation prior. A voxel-wise statistical analysis was performed on the white matter skeleton to evaluate differences of group mean value of FA and PVFs in each voxel. A general linear model was applied on the analysis under the assumption that the response associated with each voxel is a weighted linear combination of one or more predictor variables. This modelling procedure was reflected in a design matrix which defined regressors of interest, and a contrast matrix which defined the comparison (group1 vs group2, group2 vs group3, group1 vs group3). We considered 'age' 'start age' 'end age' and 'motion score' (a measurement of the degree of head motion during the scan) as the covariates included in the design matrix. A permutation testing was performed for statistical analysis in our research implemented by the function Randomise [48]) in FSL. A p-value (two-sided) smaller than 0.05 was considered significant.

Chapter 4

Results

4.1 Reference framework

4.1.1 The modified TBSS analysis

Figure 8 shows the overlay of mean FA map of all subjects, after each subject has been aligned to a common space. The mean FA, shown in red-yellow, was thresholded at 0.2 and overlaid onto the FMRIB58_FA template. The mean FA skeleton, shown in blue-light blue, was thresholded at 0.2.

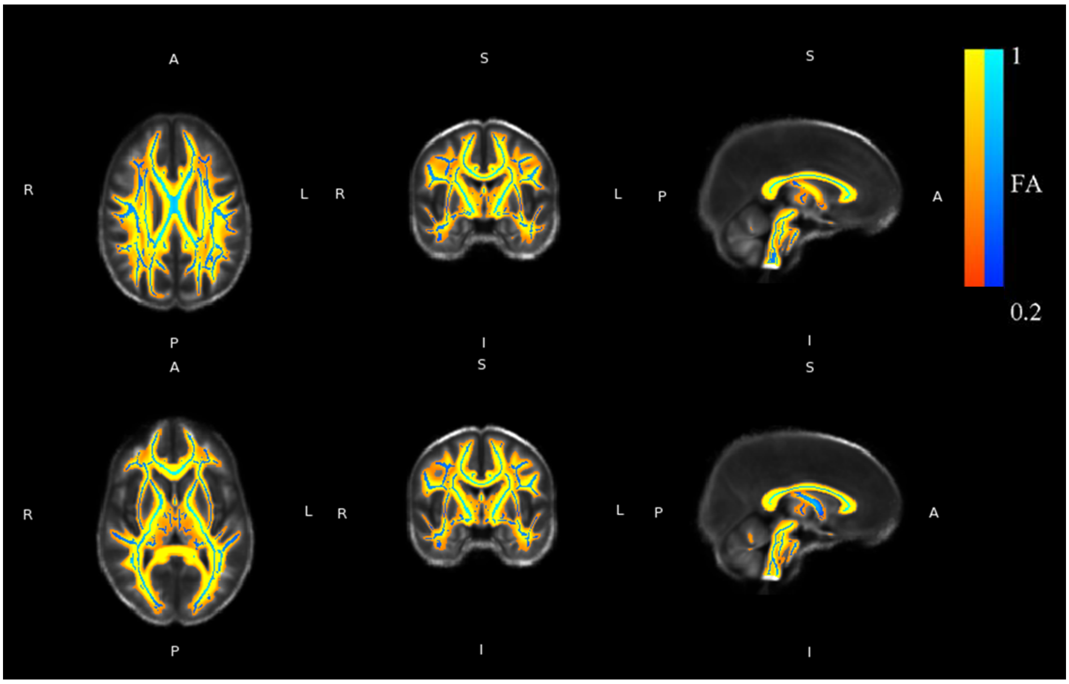

Figure 8: The mean FA value map (in red-yellow) and the FA skeleton of (in blue-lightblue) all subjects. The mean FA was thresholded at 0.2 and overlaid onto the FMRIB58_FA template (the background). The labels of the orientations of the brain image are right-left (R-L), posterior-anterior (P-A) and inferior-superior (I-S).

4.1.2 Registration by Elastix

From the result of voxel-wise statistical analysis, significant differences in FA were not observed between groups of patients treated without MPH, with short/long term

MPH. Under the choice of NCC/MI as cost functions with different sampler sizes, no significant differences were found (all p>0.2).

4.2 Proposed framework

4.2.1 Construction of the fiber orientation atlas

The fiber orientation atlas, constructed from all 84 subjects, is visualized in Figure 9 and Figure 10. Figure 9 shows the orientation atlas of the average primary fiber population. Figure 10 shows the orientation atlas of the average secondary fiber population. From the orientation atlas we can observe the average fiber populations are relatively smooth and are approximately left-right symmetric. And it appears anatomically plausible from an overview, for example, the region of corpus callosum in the first row of Figure 9, because corpus callosum is a single-fiber tract connecting two hemispheres. In both figures we used the mean FA image of overall subjects as the background to modulate the fiber orientation atlas in RGB mode, which means that red corresponds with left-right, green with posterior-anterior and blue with inferior-superior directions.

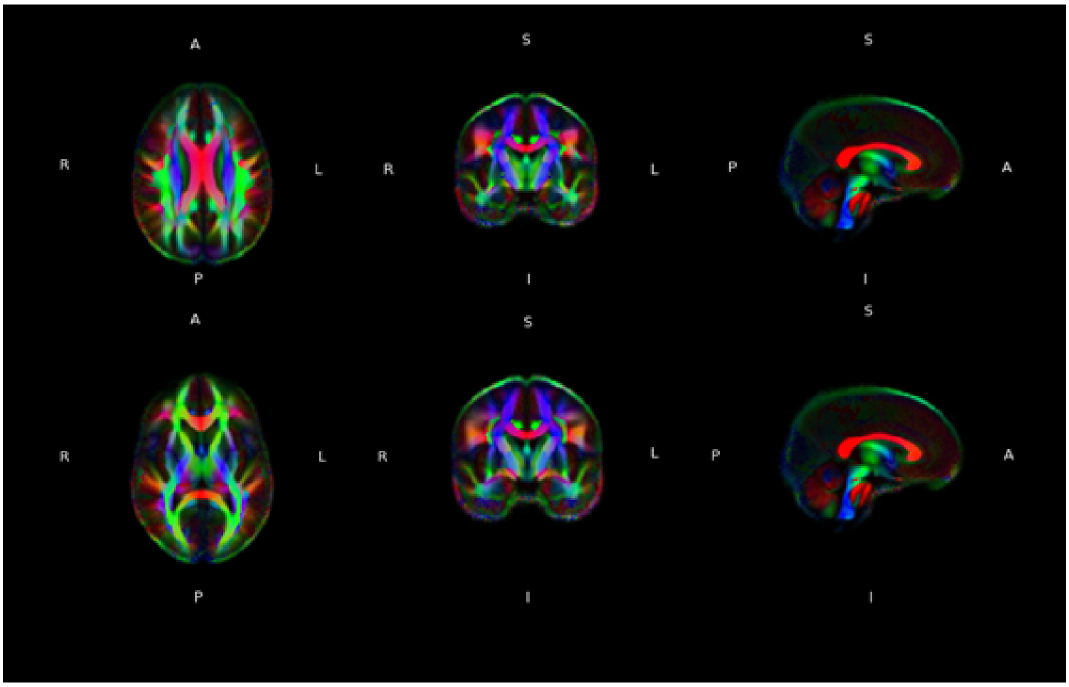

Figure 9: The orientation atlas of the primary fiber population. The fiber orientations modulate the background FA image, such that red corresponds with left-right, green with posterior-anterior and blue with inferior-superior. The first row and the second row stand for the view of two different slices in the brain.

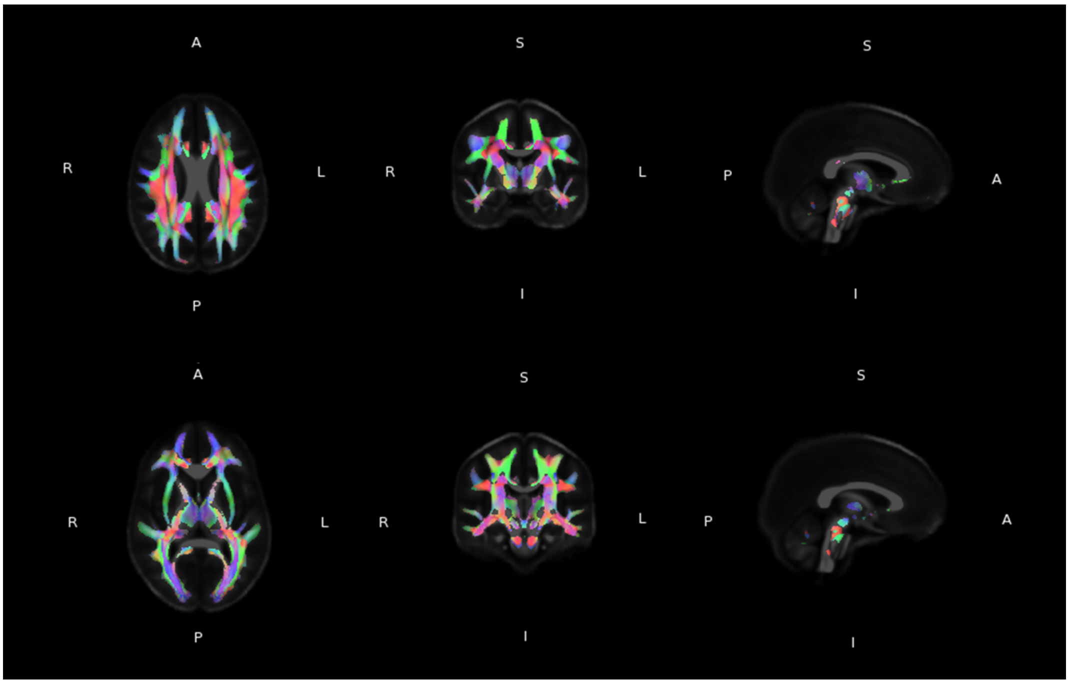

Figure 10: The orientation atlas of the secondary fiber population. The fiber orientations modulate the background FA image. Red corresponds with left-right, green with posterior-anterior and blue with inferior-superior.

4.2.2 Computation of the complexity atlas

Figure 11 shows the model complexity atlas constructed from 84 subjects in our dataset. The background is the group mean FA image. For the purpose of visualization, the average number of fiber populations was binned into four categories: blue, blue-light blue, pink, red, which stands for the regions with decreasing numbers of fiber populations. We consider a threshhold of 1.5 to obtain a discrete model complexity atlas so that areas with a population number above 1.5 indicate the crossing-fiber region (red and pink areas in Figure 11). From the complexity atlas we can observe the single-fiber areas corresponding to white matter structures known to contain a single fiber population, e.g. the corpus callosum.

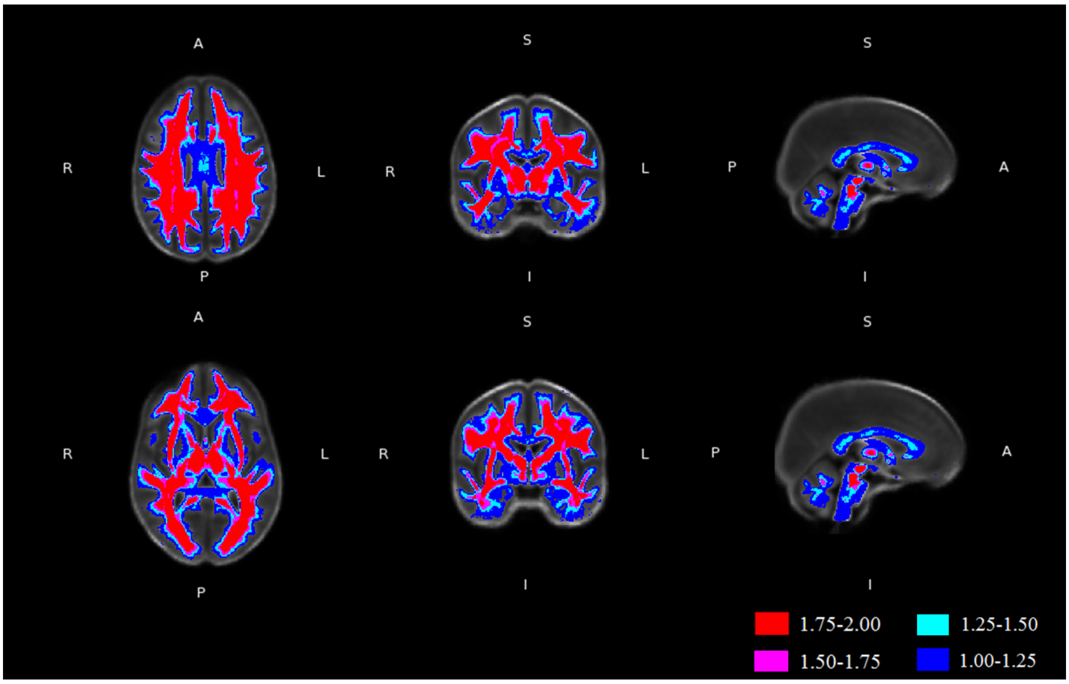

Figure 11: The average number of fiber populations per voxel in the common space. Voxels with (on average) fewer than 1 fiber tract are masked black. The background is the overall mean FA image.

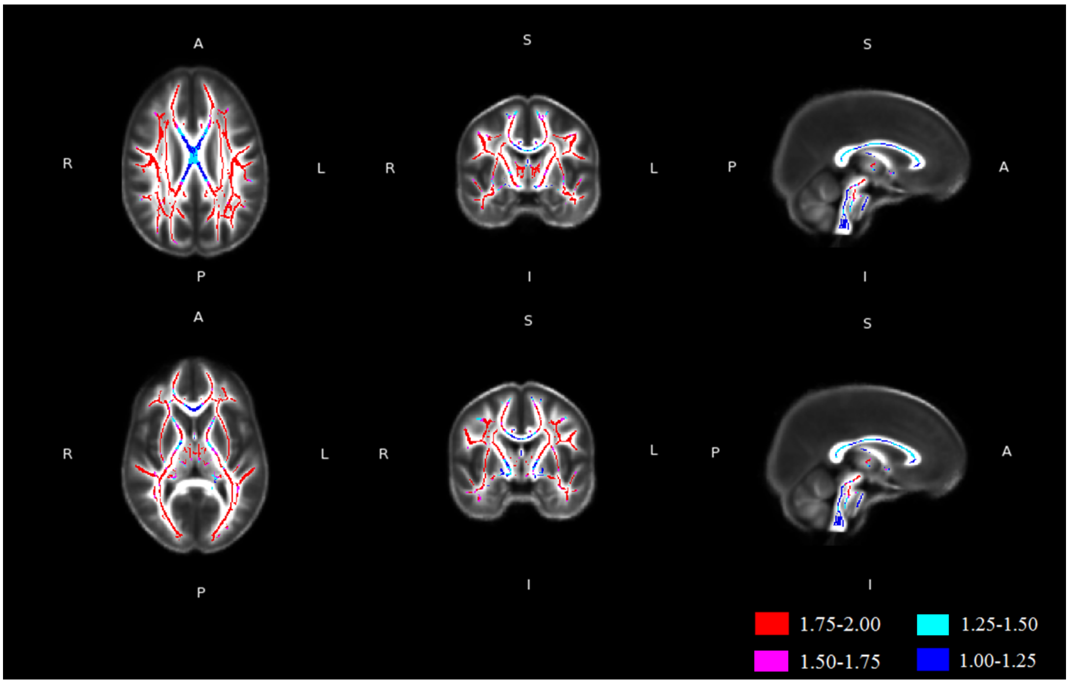

Figure 12: The average number of fiber populations per voxel on the white matter skeleton. The background is the overall mean FA image.

After masking with the mean FA skeleton, we got the complexity atlas on the skeleton in Figure 12. Based on both Figure 11 and Figure 12, we see that the crossing-fiber regions are approximately left-right symmetric. In our model complexity atlas, 91% of the white matter skeleton consists of crossing-fiber voxels.

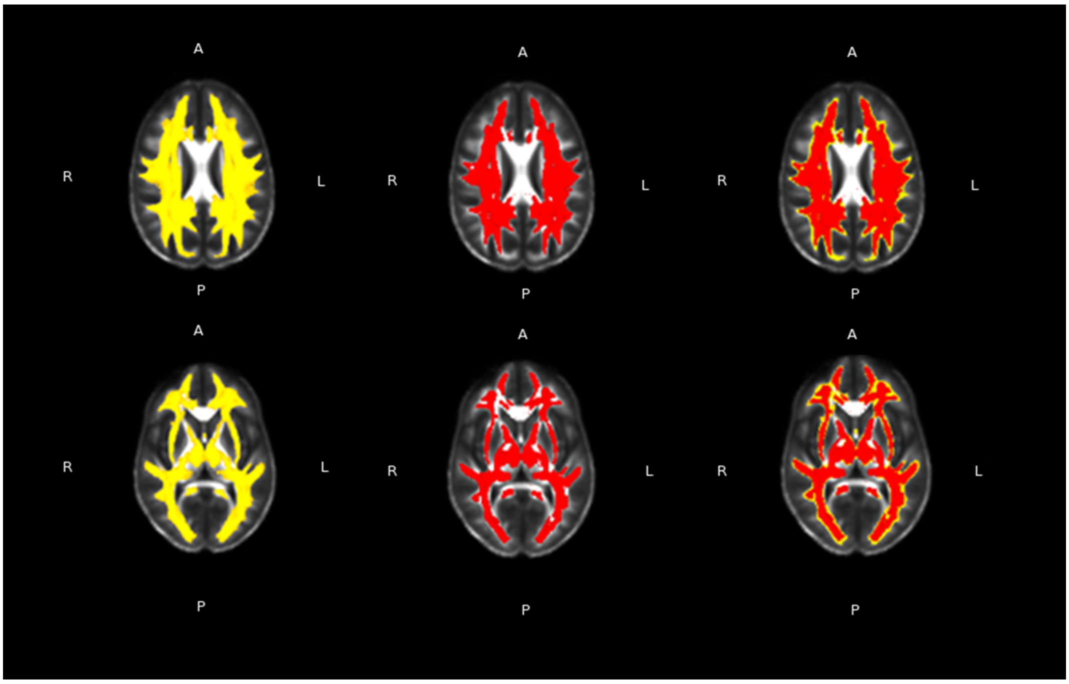

Figure 13: The comparison between the previous complexity atlas (in yellow) and the rebuilt atlas (in red) in the crossing-fiber region. The crossing-fiber region is the area with a mean number of fiber populations above 1.5.

4.2.3 An alternative way to build the complexity atlas

Additionally, we built the complexity atlas in a different way, which based on the partial volume fractions (PVFs) of fibers after model estimation with the orientation prior, stated in Section 3.3.6. Figure 13 shows the crossing-fiber region of previous complexity atlas (in yellow) and rebuilt complexity atlas (in red) as well as the comparison of both of them (the third column). We refer to the region with a mean number of fiber populations above 1.5 as the crossing-fiber region. It shows some differences on the border of the crossing-fiber region. The number of voxels of crossing fiber region in the rebuilt atlas is 80% size of the number in the previous atlas. This fraction turns to 90% if only considering the skeleton area.

4.2.4 Optimising the orientation prior

During the construction of fiber orientation atlas, in each voxel the standard deviations of primary and secondary fiber orientations around the mean fiber orientation were calculated, see Figure 14. The curve shows the ascending sorting of the standard deviations (in degree) for all the voxels on the skeleton and on the crossing-fiber area of the skeleton (Figure 14). If a fixed width of the orientation prior (σ_θ) of 20° is chosen (20° is the default setting of the toolbox fit_MRI) for the diffusion model fitting, 93% of voxels for the primary fiber populations are under this constrain while the fraction decreases to 43% for the secondary fiber populations.

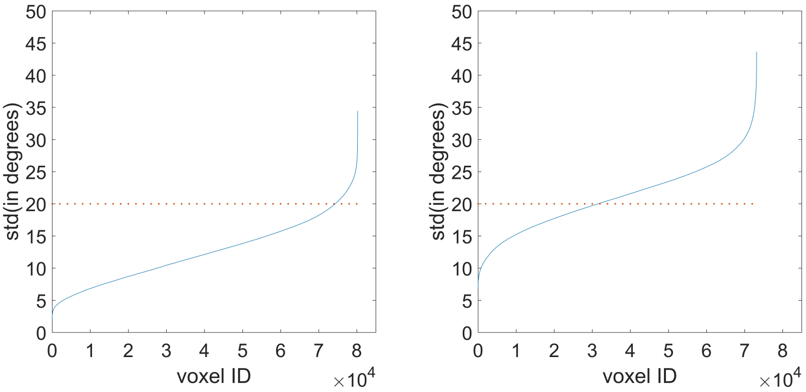

Figure 14: Left: the standard deviation of primary fiber orientations of all subjects around the mean fiber orientation in each voxel. Right: the standard deviation of secondary fiber orientations of all subjects around the mean fiber orientation in each voxel. The 'voxelID' means the name of each voxel (voxel 1, voxel 2, ... , voxel n) if we have n voxels in total. The red line means choosing 20° as the width of prior, which is the default setting in fit_MRI toolbox.

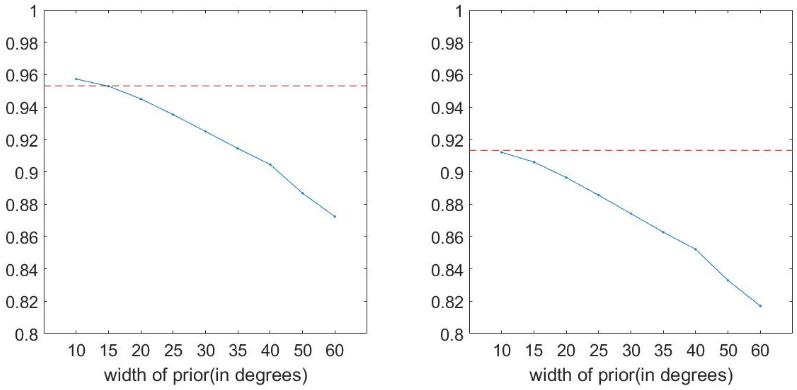

Figure 15: Left: average ICC on the TBSS skeleton, for the measurement of f1. Right: average ICC in crossing-fiber regions of the TBSS skeleton, for the measurement of f1. The red dashed lines denote the ICC under fitting with a localised width, each point in the blue lines denotes the ICC under fitting with each fixed prior width.

We optimised the orientation prior with a localised σ_θ based on the distributions shown above. We have produced four reproducibility datasets and for each reproducibility dataset we fitted with an orientation prior with a localised width as well as different fixed width of σ_θ from 10° to 60°. We measured the voxel-wise PVFs for each subject in each reproducibility dataset. Figure 15 shows the intraclass correlation coefficient (ICC) as a function of the width of σ_θ (blue curve) and the ICC when using the localised width of σ_θ (red line). Each point was calculated by the average of the ICC on the skeleton for PVFs of the primary fiber populations (f_1) and on the crossing-fiber regions of the skeleton for PVFs of the secondary fiber populations (f_2). We see that fitting with localised width of σ_θ improves the ICC without introduces too much prior information on the fiber orientations, compared with using a fixed width of σ_θ. All the ICCs under the usage of consistent model selection show a high value, proving a consistent estimation of fiber properties.

4.2.5 Statistical analysis on white matter tracts

In the permutation test, no significant differences were found between the groups. For the voxel-wise analysis of f1, no significant differences were found (all p>0.1). For the situation of f2, no significant differences were found (all p>0.15). Similarly, no significant differences were found (all p>0.1) under the application of the complexity atlas we proposed and under the application of the optimised orientation prior.

4.3 The short-term effect of MPH: a following study of CMS

After achieving the research aim of studying long-term MPH effect, we furthered our study. In the long-term MPH study, under the application of proposed framework (consistent model selection based on the ball-and-sticks model), we provided appropriate and consistent estimation of fiber-crossings. Thus we expect to find improved statistical power in the crossing-fiber region, compared with the analysis in the reference framework (based on the single tensor model). We didn't find any significant differences in both the reference and proposed framework, so we didn't see the improved statistical power, which is one of the limitations in the study of our dataset. To further our research and show the improved statistical power, we apply both frameworks on a different dataset.

In this dataset, we have found evidence that short-term MPH treatment is related to bigger white matter changes in children than in adults with ADHD after a short-term use [10]. The duration of MPH is 4 months. We expect improved statistical power after applying the pipeline of consistent model selection, to give more adequate clinical instruction. In our study population, the patients are divided into two groups, the children group (age:10.06-13.08) and the adult group (age:22.44-39.37). Each patient received MRI scanning before and after the treatment. After the application of the reference framework (based on single tensor model), we got the skeletonised

FA data for each subject. After the application of the proposed framework (based on CMS), we got the skeletonised f1/f2 data for each subject based on the fitting with orientation prior. f1/f2 refer to the volume fraction of primary/secondary fiber populations in each voxel. We made a subtraction between the skeletonised data from scanning before and after MPH use for each subject to obtain the difference of white matter tract induced by MPH. Then we applied the voxel-wise statistical analysis to compare the difference on the white matter caused by MPH for children and adult patients.

Figure 16 shows that the result of voxel-wise statistical analysis. It shows significant areas in the analysis that MPH treatment is related to bigger white matter changes in children than in adults. In the analysis with FA based on the single tensor model, the images in the top row show areas with significant differences. In the analysis with f1 based on the CMS, the images in the bottom row show areas with significant difference. No significant difference was found in the analysis of f2. We found an increase number of voxels in the significant area in f1 analysis (5656 voxels) than in FA analysis (4683 voxels). In f1 analysis, 74% of the significant voxels are in the crossing-fiber regions.

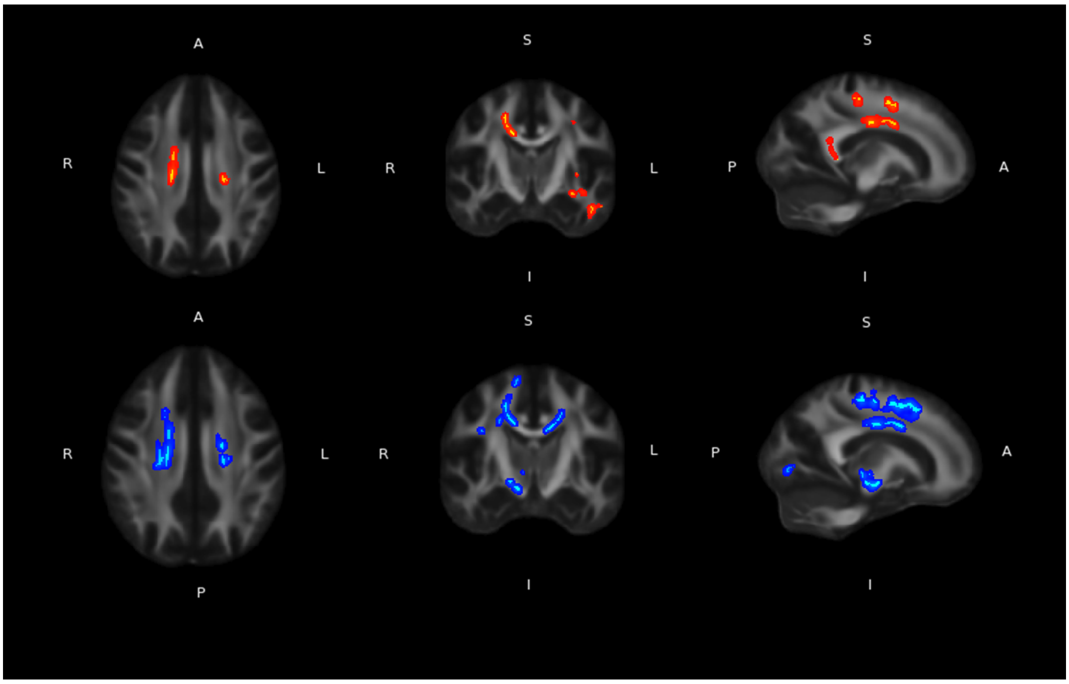

Figure 16: The significant areas where MPH caused bigger changes on the white matter skeleton of children patients than the adult patients. Top row: significant area under FA analysis based on single tensor model. Bottom row: significant area under f1 analysis based on CMS. The significant areas are thickened for visualization propose. Background is the mean FA image.

In this research, we found an improved statistical power under the application of consistent model selection. It gives evidence that the CMS is a powerful pipeline to model the fiber-crossing and improve statistical power. The significant areas we found in FA analysis were association fibers (parts of left superior longitudinal fasciculus, inferior longitudinal fasciculus, inferior fronto-occipital fasciculus) [10], which are rich in crossing fibers. So our result based on the improve statistical power in crossing fibers is valuable to give an adequate clinical instruction for the short-term medication use.

Chapter 5

Discussion

5.1 Reference framework

5.1.1 Registration by Elastix

In the reference framework, the main point was to modify the standard TBSS pipeline with a different registration. The registration was modified by using a high-dimensional registration with Elastix and leaving out the projection step. We don't establish a criterion to evaluate registration, because the registration parameters are all recommended settings according to [23]. Another reason is that we do not have a ground truth for establishing anatomical correspondence of white matter tracts for the aligned images. The fitting based on the single tensor model has limitations stated in Section 2.5.1, thus further study based on advanced model fitting should be focused to investigate the existence of significant statistical results.

5.2 Proposed framework

We applied a framework of consistent model selection (CMS) based on the ball-and-sticks model in the proposed framework. There are two main novelties in CMS. The first novelty is the introduction of fiber orientation atlas, which provided a consistent labeling of fiber populations in the crossing-fiber regions. The second novelty is a model complexity atlas, to determine the number of fiber populations in each voxel across all the subjects.

5.2.1 Construction of the fiber orientation atlas

The orientation atlas was constructed based on our dataset. It reflects not only the anatomical presence of a fiber crossing, but also the DW-MRI acquisition protocol. The modelling of fiber properties were influenced by the imaging protocol including the resolution, the number of diffusion-encoding gradient directions and the used b-values [9]. In the research of Arkesteijn et al [3], it was shown that 67% of voxels on the white matter skeleton belonged to the crossing-fiber region, while in our case the fraction increased to 91%. The main reason is the advanced imaging protocol of our data, leading to a better sensitivity of fitting in the crossing-fiber regions. For example, all subjects were scanned on a 3.0 Tesla MRI scanner with a voxel size of 2 mm x 2 mm x 2 mm and 32 non-collinear gradient directions, while in Arkesteijn's case, the data was acquired with 1.5 Tesla scanner with a voxel size of 2.2 mm x 3.3 mm x 3.5 mm and 25 gradient directions.

It is the second time the framework of consistent model selection is applied, after an improved consistent modelling of fiber-crossings shown in the research of Arkesteijn et al [3]. However, in this work a different patient population is investigated. We have 84 subjects (Age: from 22 to 40) with ADHD (part of subjects with medication), while Arkesteijn's dataset has 500 subjects (Age: from 65 to 90), free of dementia. We have a different imaging acquisition protocol compared with Arkesteijn's data (discussed in more details below). From the anatomical reasonable result of orientation atlas (Figure 9, 10) and the high ICC in Figure 15, we can see that the CMS works well as expected. We have given more evidence on the generalizability of the CMS.

5.2.2 Computation of the complexity atlas

From the model complexity atlas (Figure 11), we find a bit overfitting in the corpus callosum (CC), which is a single-fiber tract connecting two hemispheres. In the CC, the mean number of fiber population appears above 1.25 (the light-blue color), which should be 1 in principle. Two reasons lead to that issue. Firstly, the total number of subjects in our data is 84, which is not a large population to realise an exact accurate majority voting during the computation of the complexity atlas. The second reason is that the subjects in our data are adults, some of which are quite young (below 25 years old). In young people's brain, the number and density of axons are extremely high (over 10^8 fibers/mm^2 in corpus callosum reported in [1]) such that the axons are in bundles and not strictly parallel. There is a chance that the model selection identified fibers in this situation as crossing-fibers.

5.2.3 An alternative way to build the complexity atlas

We modify the way to calculate the model complexity atlas based on the partial volume fractions (PVFs) of fibers produced after fitting the data with an orientation prior. In Figure 13, 20% of voxels in crossing-fiber region differ between the complexity atlas and the rebuilt one. The differences come from the different estimated PVFs, since fitting with an orientation prior can provide a consistent labelling and enhance the modelling of PVFs especially for the secondary fiber populations. Consequently, majority voting of number of fiber populations based on PVFs shows a different result in the crossing-fiber region. In principle, we recommend applying the rebuilt complexity atlas.

5.2.4 Optimizing the orientation prior

Figure 7 shows the framework of our reproducibility study. In each voxel across four reproducibility datasets, the differences come from part of DWI volumes with different diffusion sensitizing gradient directions and different noise level. In Arkesteijn's research, the width of orientation prior (σ_θ) was selected as 25° for a good trade-off between improving the ICC without introducing too much prior information on the fiber [3]. The choice of a fixed value for the width of σ_θ is not suitable. From Figure 14 we can see a non-uniform distribution of the included angle between fiber orientation from each subject and mean fiber orientation in each voxel. For a voxel with a standard deviation much smaller than 20°, the fitting was under constrained. Similarly, the fitting was over constrained for a voxel with a standard deviation much larger than 20°. According to this distribution, we have introduced an optimised orientation prior to set a different width of σ_θ in each voxel, to give an adequate constraint and thus more consistent estimation of fiber orientations. In Figure 15, it shows a much higher ICC under the usage of this optimised prior, which also proves the consistent fiber estimation of the consistent model selection.

5.2.5 Statistical analysis on white matter tracts

Based on the consistent model selection followed by modified TBSS analysis, we got the skeletonised PVFs and applied the voxel-wise statistical analysis, same as the one in reference work. No significant differences were found between the groups. In Group2, patients started medication from an adolescent age (9.1 years old on average) until they became adults (19.8 years old on average). This group is the long-term medication research based on [10] in which we found a deviation of brain development for children under 4-month medication. In our result, it suggests that there is no significant differences on the white matter skeleton among the ADHD adult subjects without medication, with long-term medication. Thus, based on our result, we did not observe the long-term effect of medication.

5.3 Limitations

There are some limitations in our research. Firstly, for the subjects in the second group of data (patients with long-term medication), there is quite a long time (6 years in average) from the last time they receive medication to the time they were scanned. This introduces a bias due to irrelevant variables. Next, the selection of diffusion models is limited to the DW-MRI acquisition used in our study (only a single b = 1000 s/mm^2 value used), which needs to be improved to distinguish additional white matter details.

In our proposed framework, the limited number of 84 subjects in our data may cause the use of an inappropriate orientation atlas. Similarly for the complexity atlas, a dataset with larger number of subjects can provide more convincing majority voting for the number of fiber populations. Incorrect number may cause over-fitting or under-fitting of the data. We should note that over-fitting of the data is reduced by regularisation under the orientation prior. If a fiber stick compartment in the ball-and-sticks model not supported by the data, the fiber orientation is expected in the direction of the orientation prior and the stick partial volume fraction (PVF) of this fiber population will be small.

Chapter 6

Conclusion

In this thesis, to analyse the long-term effect of MPH on white matter skeleton of ADHD adult patients, two frameworks were applied. Based on all the voxel-wise statistical analysis, we did not find any significant differences on the skeletons between the three groups of patients. No long-term effect of MPH was observed. We proposed the pipeline of consistent model selection to model the fiber-crossings in the white matter, with our improvements including the alternative way to build the complexity atlas and the introduction of the optimised orientation prior.

Bibliography

[1] Francisco Aboitiz, Arnold B Scheibel, Robin S Fisher, and Eran Zaidel. Fiber composition of the human corpus callosum. *Brain research*, 598(1-2):143–153, 1992.

[2] Andrew L Alexander, Khader M Hasan, Mariana Lazar, Jay S Tsuruda, and Dennis L Parker. Analysis of partial volume effects in diffusion-tensor MRI. *Magnetic Resonance in Medicine*, 45(5):770–780, 2001.

[3] Joor Arkesteijn. *Application of Sophisticated Models to Conventional Diffusion-Weighted MRI Data*. PhD thesis, Delft University of Technology, 2018.

[4] Yaniv Assaf and Peter J Basser. Composite hindered and restricted model of diffusion (CHARMED) MR imaging of the human brain. *Neuroimage*, 27(1):48–58, 2005.

[5] Peter J Basser and Derek K Jones. Diffusion-tensor MRI: theory, experimental design and data analysis–a technical review. *NMR in Biomedicine*, 15(7-8):456–467, 2002.

[6] Peter J Basser, James Mattiello, and Denis LeBihan. MR diffusion tensor spectroscopy and imaging. *Biophysical journal*, 66(1):259–267, 1994.

[7] Mark F Bear, Barry W Connors, and Michael A Paradiso. *Neuroscience*, volume 2. Lippincott Williams & Wilkins, 2007.

[8] Christian Beaulieu. The basis of anisotropic water diffusion in the nervous system–a technical review. *NMR in Biomedicine*, 15(7-8):435–455, 2002.

[9] Timothy EJ Behrens, H Johansen Berg, Saad Jbabdi, Matthew FS Rushworth, and Mark W Woolrich. Probabilistic diffusion tractography with multiple fibre orientations: What can we gain? *Neuroimage*, 34(1):144–155, 2007.

[10] Cheima Bouziane. , Olena G Filatova, Anouk Schrantee, Matthan WA Caan, Frans M Vos, Liesbeth Reneman, Effects of Methylphenidate on the Human White Matter in Children vs Adults with Attention-Deficit/Hyperactivity Disorder: A Randomized Clinical Trial. *submitted*, 2018.

[11] Robert Brown. XXVII. A brief account of microscopical observations made in the months of June, July and August 1827, on the particles contained in the pollen of plants; and on the general existence of active molecules in organic and inorganic bodies. *The Philosophical Magazine*, 4(21):161–173, 1828.

[12] Matthan WA Caan, H Ganesh Khedoe, Dirk HJ Poot, J Arjan, Silvia D Olabarriaga, Kees A Grimbergen, Lucas J Van Vliet, and Frans M Vos. Estimation of diffusion properties in crossing fiber bundles. *IEEE transactions on medical imaging*, 29(8):1504–1515, 2010.

[13] Kathleen M Curran, Louise Emsell, and Alexander Leemans. Quantitative DTI measures. In *Diffusion Tensor Imaging*, pages 65–87. Springer, 2016.

[14] Marius de Groot, Meike W Vernooij, Stefan Klein, M Arfan Ikram, Frans M Vos, Stephen M Smith, Wiro J Niessen, and Jesper LR Andersson. Improving alignment in tract-based spatial statistics: evaluation and optimization of image registration. *Neuroimage*, 76:400–411, 2013.

[15] Erwin L Hahn. Spin echoes. *Physical review*, 80(4):580, 1950.

[16] Luis Ibanez, William Schroeder, Lydia Ng, and Josh Cates. The ITK software guide. 2005.

[17] Saad Jbabdi, Timothy EJ Behrens, and Stephen M Smith. Crossing fibres in tract-based spatial statistics. *Neuroimage*, 49(1):249–256, 2010.

[18] Mark Jenkinson, Christian F Beckmann, Timothy EJ Behrens, Mark W Woolrich, and Stephen M Smith. Fsl. *Neuroimage*, 62(2):782–790, 2012.

[19] Peter S Jensen. A 14-month randomized clinical trial of treatment strategies for attention-deficit/hyperactivity disorder. *Archives of general psychiatry*, 56(12):1073–1086, 1999.

[20] Ben Jeurissen, Alexander Leemans, Jacques-Donald Tournier, Derek K Jones, and Jan Sijbers. Investigating the prevalence of complex fiber configurations in white matter tissue with diffusion magnetic resonance imaging. *Human brain mapping*, 34(11):2747–2766, 2013.

[21] Derek K Jones, Thomas R Knösche, and Robert Turner. White matter integrity, fiber count, and other fallacies: the do's and don'ts of diffusion mri. *Neuroimage*, 73:239–254, 2013.

[22] S Klein and M Staring. Elastix: the manual, 2015.

[23] Stefan Klein, Marius Staring, Keelin Murphy, Max A Viergever, and Josien PW Pluim. Elastix: a toolbox for intensity-based medical image registration. *IEEE transactions on medical imaging*, 29(1):196–205, 2010.

[24] Stefan Klein, Marius Staring, and Josien PW Pluim. Evaluation of optimization methods for nonrigid medical image registration using mutual information and B-splines. *IEEE transactions on image processing*, 16(12):2879–2890, 2007.

[25] BW Kreher, JF Schneider, I Mader, E Martin, J Hennig, and KA Il'Yasov. Multi-tensor approach for analysis and tracking of complex fiber configurations. *Magnetic resonance in medicine*, 54(5):1216–1225, 2005.

[26] Denis Le Bihan, Jean-François Mangin, Cyril Poupon, Chris A Clark, Sabina Pappata, Nicolas Molko, and Hughes Chabriat. Diffusion tensor imaging: concepts and applications. *Journal of magnetic resonance imaging*, 13(4):534–546, 2001.

[27] Denis Le Bihan, Cyril Poupon, Alexis Amadon, and Franck Lethimonnier. Artifacts and pitfalls in diffusion MRI. *Journal of magnetic resonance imaging*, 24(3):478–488, 2006.

[28] Alexander Leemans and Derek K Jones. The B-matrix must be rotated when correcting for subject motion in DTI data. *Magnetic resonance in medicine*, 61(6):1336–1349, 2009.

[29] Hava Lester and Simon R Arridge. A survey of hierarchical non-linear medical image registration. *Pattern recognition*, 32(1):129–149, 1999.

[30] Bostjan Likar and Franjo Pernuš. A hierarchical approach to elastic registration based on mutual information. *Image and vision computing*, 19(1-2):33–44, 2001.

[31] P Mukherjee, JI Berman, SW Chung, CP Hess, and RG Henry. Diffusion tensor MR imaging and fiber tractography: theoretic underpinnings. *American journal of neuroradiology*, 29(4):632–641, 2008.

[32] Dirk HJ Poot and Stefan Klein. Detecting statistically significant differences in quantitative MRI experiments, applied to diffusion tensor imaging. *IEEE transactions on medical imaging*, 34(5):1164–1176, 2015.

[33] Jerry L Prince and Jonathan M Links. *Medical imaging signals and systems*. Pearson Prentice Hall Upper Saddle River, 2006.

[34] Daniel Rueckert, Luke I Sonoda, Carmel Hayes, Derek LG Hill, Martin O Leach, and David J Hawkes. Nonrigid registration using free-form deformations: application to breast mr images. *IEEE transactions on medical imaging*, 18(8):712–721, 1999.

[35] Armin Schwartzman, Robert F Dougherty, and Jonathan E Taylor. Cross-subject comparison of principal diffusion direction maps. *Magnetic Resonance in Medicine*, 53(6):1423–1431, 2005.

[36] Shayle R Searle and Marvin HJ Gruber. *Linear models*. John Wiley & Sons, 2016.

[37] Stephen M Smith. Fast robust automated brain extraction. *Human brain mapping*, 17(3):143–155, 2002.

[38] Stephen M Smith, Mark Jenkinson, Heidi Johansen-Berg, Daniel Rueckert, Thomas E Nichols, Clare E Mackay, Kate E Watkins, Olga Ciccarelli, M Zaheer Cader, Paul M Matthews, et al. Tract-based spatial statistics: voxelwise analysis of multi-subject diffusion data. *Neuroimage*, 31(4):1487–1505, 2006.

[39] Edward O Stejskal and John E Tanner. Spin diffusion measurements: spin echoes in the presence of a time-dependent field gradient. *The journal of chemical physics*, 42(1):288–292, 1965.

[40] Mohammadkazem Tarzamni, Ali Kiani Nazarlou, and Jamil Abdolmohammadi. MRI imaging and pancreatic diseases. *Acta healthmedica*, 1:8–12, 2016.

[41] Philippe Thévenaz, Michel Bierlaire, and Michael Unser. Halt on sampling for image registration based on mutual information. *Sample Theory Signal Image Process*, 7(2), 2008.

[42] Philippe Thévenaz, Thierry Blu, and Michael Unser. Interpolation revisited [medical images application]. *IEEE Transactions on medical imaging*, 19(7):739–758, 2000.

[43] Henry C Torrey. Bloch equations with diffusion terms. *Physical review*, 104(3):563, 1956.

[44] David S Tuch. Q-ball imaging. *Magnetic resonance in medicine*, 52(6):1358–1372, 2004.

[45] David S Tuch, Timothy G Reese, Mette R Wiegell, Nikos Makris, John W Belliveau, and Van J Wedeen. High angular resolution diffusion imaging reveals intravoxel white matter fiber heterogeneity. *Magnetic resonance in medicine*, 48(4):577–582, 2002.

[46] Claudia AM Wheeler-Kingshott and Mara Cercignani. About “axial” and “radial” diffusivities. *Magnetic resonance in medicine*, 61(5):1255–1260, 2009.

[47] Timothy E Wilens and Thomas J Spencer. Understanding attention-deficit/hyperactivity disorder from childhood to adulthood. *Postgraduate medicine*, 122(5):97–109, 2010.

[48] Anderson M Winkler, Gerard R Ridgway, Matthew A Webster, Stephen M Smith, and Thomas E Nichols. Permutation inference for the general linear model. *Neuroimage*, 92:381–397, 2014.

[49] Gavin P Winston. The physical and biological basis of quantitative parameters derived from diffusion MRI. *Quantitative imaging in medicine and surgery*, 2(4):254, 2012.

[50] Hui Zhang, Brian B Avants, Paul A Yushkevich, John H Woo, Sumei Wang, Leo F McCluskey, Lauren B Elman, Elias R Melhem, and James C Gee. High-dimensional spatial normalization of diffusion tensor images improves the detection of white matter differences: an example study using amyotrophic lateral sclerosis. *IEEE transactions on medical imaging*, 26(11):1585–1597, 2007.

[51] Hui Zhang, Torben Schneider, Claudia A Wheeler-Kingshott, and Daniel C Alexander. NODDI: practical in vivo neurite orientation dispersion and density imaging of the human brain. *Neuroimage*, 61(4):1000–1016, 2012.

[52] Hui Zhang, Paul A Yushkevich, Daniel C Alexander, and James C Gee. Deformable registration of diffusion tensor MR images with explicit orientation optimization. *Medical image analysis*, 10(5):764–785, 2006.